Analytical bond order potential for simulations of BeO 1D and 2D nanostructures and plasma-surface interactions

J Byggmästar, E A Hodille, Y. Ferro, K. Nordlund

Analytical bond order potential for simulations of BeO 1D and 2D nanostructures and plasma-surface interactions

J Byggmästar[1], E A Hodille[2], Y Ferro[2] and K Nordlund[1]

[1] Department of Physics, P.O. Box 43, FI-00014 University of Helsinki, Finland
[2] Aix-Marseille Université-CNRS, PIIM UMR 7345, 13397 Marseille, France

E-mail: jesper.byggmastar@helsinki.fi

Abstract. An analytical interatomic bond order potential for the Be–O system is presented. The potential is fitted and compared to a large database of bulk BeO and point defect properties obtained using density functional theory. Its main applications include simulations of plasma-surface interactions involving oxygen or oxide layers on beryllium, as well as simulations of BeO nanotubes and nanosheets. We apply the potential in a study of oxygen irradiation of Be surfaces, and observe the early stages of an oxide layer forming on the Be surface. Predicted thermal and elastic properties of BeO nanotubes and nanosheets are simulated and compared with published ab initio data.

Keywords: interatomic potential, beryllium, oxygen, molecular dynamics

Submitted to: *J. Phys.: Condens. Matter*

1. Introduction

The plasma-facing materials in future fusion reactors must be able to withstand extreme conditions due to high thermal loads, ion fluxes, and neutron irradiation. Beryllium has been selected as the first-wall material of ITER. The properties contributing to the choice of Be include a low atomic mass (and hence low plasma contamination), low tritium retention, and its oxygen gettering ability [1]. The behaviour of Be under fusion-relevant conditions has therefore been extensively studied in experimental and modelling work [2, 3, 4, 5]. However, little is known about the effects of oxygen on the structural and erosion properties of the Be walls [6, 7]. The high affinity for oxygen is likely to lead to a growing plasma-facing oxide layer if exposed to air, with subsequent erosion and sputtering of oxide molecules. Addressing the consequences of the otherwise desirable oxygen gettering ability of Be is therefore crucial.

Beryllium oxide has also recently gained considerable interest within the nanomaterials community, due to the partly covalent bonding nature of the otherwise ionic compound. Ever since the discovery of single layered carbon nanostructures, nanotubes and nanosheets of carbon and other materials have been intensively studied for their exceptional electronic and mechanical properties [8, 9]. The possibility of producing carbon-like sp^2-bonded BeO nanostructures has been recently proposed [10], and been the subject of a number of first-principles studies [10, 11, 12, 13, 14, 15, 16, 17].

Molecular dynamics (MD) simulations are a useful tool for studying atomic processes on time and length scales inaccessible to experiments and density functional theory, such as sputtering mechanisms or radiation damage production. The accuracy of MD simulations is directly defined by the interatomic potential used to describe the interactions between individual atoms. Developing accurate many-body interatomic potentials for different materials is therefore an essential part of atomistic modelling, and no many-body potential has to our knowledge been developed for the Be–O system. A many-body potential for the Be–O system will allow simulations of both fusion-relevant plasma-surface interactions with oxide layer formation and erosion as well as simulations of mechanical and thermal stability of BeO nanostructures.

The potential formalism used here was originally developed by Tersoff [18, 19], using the concept of bond order as discussed by Abell [20]. Despite being originally developed to model covalently bonded materials, the potential has been shown to closely resemble the embedded atom method potentials used for metals [21, 22]. The bond order formalism therefore allows modelling of differently bonded materials, from pure metals to e.g. metal and semiconductor compounds. The potential function used in this work, referred to as the analytical bond order potential (ABOP), is similar to the original form by Tersoff, but slightly extended and rewritten. The potential is capable of modelling bond breaking and forming, and has been previously applied to a wide variety of materials, including pure metallic, metal–carbon–hydrogen, and metal–oxygen systems [23, 24, 25, 26, 27, 28, 29]. In this work, we extend previously developed potentials for the fusion-relevant Be–W–C–H materials [25, 28, 30, 31] to include the Be–O interaction.

The article is structured as follows. In section 2, we briefly describe the functional form of the ABOP, and the strategy used for fitting the potential to the constructed database of material properties. In section 3, we summarise the accuracy of the fitted properties of the potential, and discuss results from testing of the potential by calculating properties not included in the fitting process. Finally, we apply the ABOP in simulations of O irradiation of a Be surface, as well as investigations of the thermal stability and elasticity of BeO nanotubes and nanosheets. Concluding remarks are given in section 4.

2. Methods

2.1. Potential formalism

The functional form and its parameters has been extensively discussed previously (see e.g. Ref. [23]), and will only be briefly presented here. The total potential energy in the ABOP is expressed as a sum over all atomic bonds, given by

$$V = \sum_i \sum_{j>i} V_{ij} = \sum_i \sum_{j>i} f_{\mathrm{C}}(r_{ij})[V_{\mathrm{R}}(r_{ij}) - \bar{b}_{ij} V_{\mathrm{A}}(r_{ij})], \quad (1)$$

where the repulsive and attractive functions form a simple Morse-like potential [32]

$$V_{\mathrm{R}}(r_{ij}) = \frac{D_0}{S-1} \exp\left[-\beta\sqrt{2S}(r_{ij} - r_0)\right] \quad (2)$$

$$V_{\mathrm{A}}(r_{ij}) = \frac{SD_0}{S-1} \exp\left[-\beta\sqrt{2/S}(r_{ij} - r_0)\right]. \quad (3)$$

D_0 and r_0 are the dimer bond energy and length. The interaction range is typically restricted to the nearest-neighbour shell by the cutoff function

$$f_C(r) = \begin{cases} 1, & r \le R - D \\ \frac{1}{2} - \frac{1}{2}\sin\left[\frac{\pi}{2D}(r-R)\right], & |R-r| \le D \\ 0, & r \ge R + D. \end{cases} \quad (4)$$

Here, R is the cutoff distance and D defines the width of the cutoff region, where the potential energy smoothly approaches zero. All many-body interactions are incorporated in the bond order function, which is written in the symmetric form

$$\bar{b}_{ij} = \frac{b_{ij} + b_{ji}}{2}, \quad (5)$$

where

$$b_{ij} = (1 + \chi_{ij})^{-1/2}. \quad (6)$$

Furthermore, χ_{ij} is given by

$$\chi_{ij} = \sum_{k(\neq i,j)} f_C(r_{ik}) g_{ik}(\theta_{ijk}) \omega_{ijk} \exp\left[\alpha_{ijk}(r_{ij} - r_{ik})\right], \quad (7)$$

and the angular function by

$$g_{ik}(\theta_{ijk}) = \gamma_{ik}\left[1 + \frac{c_{ik}^2}{d_{ik}^2} - \frac{c_{ik}^2}{d_{ik}^2 + (h_{ik} + \cos\theta_{ijk})^2}\right]. \quad (8)$$

In simulations involving high kinetic energies, such as irradiation studies, the repulsive part of the potential given above is unphysically weak and must be modified to describe repulsive short-range interactions more accurately. A common approach is to join the universal repulsive Ziegler-Biersack-Littmark potential [33], $V_{\mathrm{ZBL}}(r_{ij})$, with the original potential V_{ij} as

$$V'_{ij} = F(r_{ij}) V_{ij} + [1 - F(r_{ij})]\, V_{\mathrm{ZBL}}. \quad (9)$$

Here, $F(r)$ is the Fermi function

$$F(r) = \frac{1}{1 + \exp[-b_{\mathrm{f}}(r - r_{\mathrm{f}})]}, \quad (10)$$

which ensures a smooth transition between the original potential and the repulsive ZBL potential. The parameters b_{f} and r_{f}, defining the transition range and distance, are chosen so that the equilibrium properties are nearly unchanged for all considered coordination numbers.

2.2. Computational details

The interatomic potential was fitted using the code TULIP [34]. Molecular dynamics simulations were carried out with the codes PARCAS [35, 36] and LAMMPS [37]. The time step required for energy conservation in the MD simulations was 0.6 fs, tested at room temperature. The irradiation simulations employ an adaptive time step according to the selection criterion in [38]. Structural optimisations, defect energies, and the phonon dispersion in the ABOP were calculated using ASE [39] and LAMMPS [37]. All density functional theory (DFT) calculations were carried out using the QUANTUM ESPRESSO code [40].

2.3. Fitting database

Beryllium oxide crystallises in the wurtzite structure at atmospheric pressure and room temperature [41, 42]. A large amount of experimental data is available for characterising BeO wurtzite: the lattice constants [43, 44, 45, 46], the cohesive energy [47], the bulk modulus [43], and the elastic constants [43, 48, 49, 50]. However, some other hypothetical Be–O structures in which the beryllium atom has different coordination numbers have to also be considered. These structures will enlarge the fitting database and ensure a better transferability of the interatomic potential to any kind of structural environment.

Consequently, DFT calculations were carried out for the Be–O dimer, a linear chain of Be–O units, a graphene-like 2D structure in which Be–O units form hexagons in a plane, and the 3D wurtzite, zinc blende, rock salt, and ceasium chloride structures. The corresponding cohesive energies, lattice constants, bulk moduli and elastic constants were determined. In addition, the formation energies of different defects in BeO wurtzite were calculated as well as the solution energies of oxygen in pure hcp Be. Surface properties were also considered by investigating the adsorption of an oxygen on the Be hcp (0001) surface. Additionally, phonon properties of BeO wurtzite were determined to assess the reliability of the ABOP.

The energy of the oxygen molecule in its ground state is required to compute the cohesive, formation, and adsorption energies discussed in this work. The ground state of the O_2 molecule is spin triplet, which consequently requires spin-polarised calculations. In addition, point defects such as the Be vacancy in BeO wurtzite displayed magnetic properties, as previously pointed out in the literature [51, 52, 53], which also requires spin-polarisation.

The DFT calculations have been performed with the GGA-PBE exchange and correlation functional [54] and ultra-soft pseudo-potentials [55]. Cutoff energies of 52 Ry (707 eV) and 416 Ry (5658 eV) were used for the truncation of the expansion of the wave functions and the electronic density, respectively. The k-point sampling has been converged to $24 \times 24 \times 24$ for the wurtzite unit cell containing 2 Be atoms and 2 O atoms. The phonon calculations were performed in the framework of the Density Functional Pertubation Theory [56] with the same cutoff energies and k-point sampling as above.

The k-point samplings for the others structures

were scaled as the inverse of the size of the box. The dimer, linear, and graphene-like structures exhibit non-periodic structures in at least one direction. Thus, in these directions, the size of the box was increased to be more than 20 Å to prevent interactions across the periodic boundaries. In these directions, only one k-point was used.

The formation energies of defects in the BeO wurtzite lattice were calculated in a $3 \times 3 \times 3$ supercell (54 Be atoms and 54 O atoms) with a k-point sampling of $6 \times 6 \times 6$. Relaxations of both the atomic positions and the volume of the cell were carried out.

The calculations of an O impurity in the Be hcp lattice and on the Be hcp (0001) surface were performed with a cutoff energy of 50 Ry (680 eV) for the wave functions and 400 Ry (5440 eV) for the electronic density. The formation energy of O was calculated in a $5 \times 5 \times 4$ Be supercell (200 Be atoms). For these calculations, the k-point sampling was $4 \times 4 \times 5$ ($20 \times 20 \times 20$ for the Be hcp unit cell with 2 Be atoms). The positions of all atoms as well as the volume of the cell were relaxed. For the surface calculations, a 3×3 supercell was used in the a and b directions (parallel to the (0001) surface). Eleven hexagonal Be layer were considered in the c direction (perpendicular to the surface) with a 24 Å vacuum layer to prevent interactions between the studied surface and the bottom of the repeated supercell in the c direction. The k-point sampling used for these calculations was $6 \times 6 \times 1$. The calculations were done by relaxing all atoms except the two bottom layers.

2.4. Fitting methods

With reference data for BeO phases in a wide range of coordination numbers from the DFT calculations, the fitting of the potential parameters followed a similar strategy as previously outlined in e.g. Ref. [23]. The cutoff range of Be–O interactions was chosen to be between the first and second nearest neighbour Be–O shells for all structures included in the fitting process. When the interaction range is restricted to nearest neighbours only, the energy per bond, E_b, follows the Pauling relation [57], given in the ABOP by

$$E_\mathrm{b} = D_0 \exp\left[-\beta\sqrt{2S}(r_\mathrm{b} - r_0)\right], \tag{11}$$

where r_b is the bond length. D_0 and r_0 are typically chosen to give the correct dimer energy and bond length, β can be calculated from the ground state frequency of the dimer, and S fitted to give the correct bond energies for the higher coordinated structures. However, the bond energy of the dimer given by DFT and experiments is weak compared to the bond energies of the higher coordinated structures, and could not be used to fix D_0. Both D_0 and r_0 were therefore included, together with S and β, when fitting equation 11 to satisfy the bond energies of all structures studied by DFT.

Care had to be taken so that the interaction range of the underlying Be–Be potential (version II from Ref. [28]) did not interfere with the above fitting strategy. Including both nearest neighbour Be–O and Be–Be interactions effectively changes the above Pauling relation for Be–O structures. The nearest neighbour Be–Be bond in the ground state of BeO (wurtzite), is 2.7 Å according to experimental data [43]. The cutoff radius of the Be–Be potential is 2.685 Å, resulting in Be–Be bonds being included after only a small compressive strain. Consequently, fitting the ABOP to the experimental lattice constants leads to a poor description of elastic properties, as the energy cost for straining the structure is highly asymmetrical around the equilibrium. In order to avoid such unphysical behaviour, the ABOP was fitted to the (slightly overestimated) lattice constants and cohesive energies obtained in the DFT calculations.

The parameters of the angular function $g_{ik}(\theta_{ijk})$ in equation 8 were numerically fitted using the reference data obtained by DFT. The parameter h, defining the optimal angle between the atoms ijk, was allowed to vary between the equilibrium angles of the lowest energy phases, wurtzite ($109.5°; h = 0.33$), and the graphene-like sheet ($120°; h = 0.5$).

3. Results and discussion

3.1. Fitted properties

Table 1 shows the properties of different BeO phases given by the ABOP and compared to data obtained by the DFT calculations and available experimental data. The potential parameters are given in table 2. The structural properties of the ground state (wurtzite) phase are well reproduced by both DFT and the ABOP, including all elastic constants. However, it should be noted that the experimental values for the elastic constants vary significantly from study to study. The lattice constants obtained in the DFT calculations are slightly overestimated compared to the experimental data, which is a known feature of the GGA-PBE functionals [58]. Nevertheless, as noted previously, the ABOP was fitted to reproduce the DFT lattice constants of the different phases, in order to get good elastic properties.

As a consequence of restricting the interactions to nearest neighbours, the ABOP formalism cannot reproduce the subtle energy difference between the wurtzite and zinc blende structures. The geometry of the nearest neighbour shell is identical in both structures, and the energy and bond distances will

Table 1: Properties of different existing and hypothetical BeO phases obtained with DFT and the ABOP, compared with available experimental results. The listed properties with units are; r_0: bond length (Å), E_{coh}: cohesive energy per atom (eV/atom), a, c: lattice constants (Å), z: internal coordinate of wurtzite, B: bulk modulus (GPa), B': pressure derivative of the bulk modulus, c_{ij}: elastic constants (GPa).

	DFT	Experiment	ABOP
BeO graphene			
r_{b}	1.591		1.605
E_{coh}	−5.353		−5.458
BeO wurtzite ($P6_3mc$, no. 186)			
a	2.766	2.698[a]	2.758
c	4.496	4.38[a]	4.503
z	0.3773	0.378[a]	0.375
E_{coh}	−5.469	−6.1[b]	−5.559
B	218	210[a], 224[c], 249[d], 208[e]	208
B'		5.1 ± 1.0[a]	4.0
c_{11}	424.4	470[c], 460.6[d], 454[e]	463
c_{12}	133.7	168[c], 126.5[d], 85[e]	98
c_{13}	96.6	119[c], 88.48[d], 77[e]	62
c_{33}	466.1	494[c], 491.6[d], 488[e]	499
c_{44}	126.6	153[c], 147.7[d], 155[e]	164
c_{66}	145.3	152[c], 167.0[d], 185[e]	183
BeO zinc blende ($F\bar{4}3m$, no. 216)			
a	3.904		3.900
E_{coh}	−5.463		−5.559
B	219		208
BeO rock salt ($Fm\bar{3}m$, no. 225)			
a	3.729		3.825
E_{coh}	−4.975		−4.075
B	225		185
BeO caesium chloride ($Pm\bar{3}m$, no. 221)			
a	2.406		2.397
E_{coh}	−3.849		−3.899
B	199		197

[a] Ref. [43] [b] Calculated from the room temperature enthalpy of formation from Ref. [47] [c] Ref. [48] [d] Ref. [49] [e] Ref. [50]

therefore be exactly the same in the ABOP. The cohesive energy and bond distance of the graphene-like BeO sheet are also in good agreement with DFT, and more importantly, the difference in cohesive energy between the wurtzite and graphene phases is in excellent agreement with DFT.

The overall good agreement between the ABOP and DFT across a wide range of coordination numbers generally ensures a good transferability to bonding geometries and coordination numbers not found in the fitted structures. In the following sections, we test this assumption by calculating properties not included in the fitting database.

3.2. Tested properties

3.2.1. BeO bulk properties. When fitting an interatomic potential to properties of a select amount of crystalline phases, it is important to confirm that the

Table 2: Parameters for the Be–O ABOP. The Be–Be and O–O parameters are taken from earlier studies (Be–Be version II from Ref. [28]), and the Be–O parameters are fitted in this study.

	Be–Be [28]	O–O [29]	Be–O
D_0	1.03571	5.166	6.783
r_0	2.07880	1.2075	1.41
β	1.3	2.3090	1.6525
S	1.88982	1.3864	1.8754
γ	8.19587×10^{-7}	0.82595	0.3940568
c	89.3894	0.035608	1.4
d	0.27443	0.046496	0.821
h	0.7606934	0.45056	0.488
R	2.535	2.1	2.5
D	0.15	0.2	0.2
α	0.0	0.0	0.0
ω	1.0	1.0	1.0
b_f	15.0	12.0	15.0
r_f	0.8	0.5	0.8

desired ground state phase is correctly predicted by the potential, and that no phase not considered in the fitting process is lower in energy. The ABOP was therefore subjected to extensive annealing and heating/quenching MD simulations of wurtzite BeO, and no recrystallisations into other phases were observed. Upon heating to temperatures above the melting point, we found that BeO melts into a very low-density liquid phase with large regions of empty space between the clusters of atoms. The melting point is commonly estimated by creating a liquid-solid interface, and determining the temperature at which the molten and crystalline phases are in equilibrium. However, due to the melting behaviour of BeO, this was not possible. We therefore carried out simple heating simulations with different heating rates to determine an approximate melting temperature. Simple heating of a single-crystalline system in MD is known to overestimate the melting point due to the the lack of nucleation points [59], and due to the extremely high heating rates required for MD time scales. The observed melting point for all tested heating rates was about 3000 K. This should be considered an upper limit predicted by the ABOP, and is therefore in good agreement with the experimental melting point of 2851 K [47].

We also determined the thermal expansion coefficients of wurtzite BeO and compared the obtained results to experimental data. The experimental data from Kozlovskii et al. [60] are for the temperature range 293 K−1823 K. Slack and Bartram [61] reviewed values in the temperature range 300 K−2200 K, which is the range on which we focused our study. Both studies reported the linear expansion, i.e. the variation of the sample in a single direction and not the variation of the volume of the sample. Since the crystal we are simulating is a single crystal, unlike the experiments, we have easily access to the linear thermal expansion coefficients, $\alpha_{i\in\{x,y,z\}}$ (in K^{-1}), of the different directions of the lattice. The appropriate coefficient to compare to the experimental data on polycrystalline BeO is then the directionally averaged value [61]

$$\widetilde{\alpha} = \frac{1}{3}(\alpha_x + \alpha_y + \alpha_z). \tag{12}$$

To obtain the thermal expansion, a cuboid box of wurtzite BeO, containing 15840 atoms was used. The temperature of the system was quickly increased from 0 K to 2000 K in 10 ps, kept constant for about 40 ps so that the volume of the box relaxed to zero pressure, and finally the temperature was decreased with a rate of 10 K/ps. The thermal expansion was determined by looking at the variation of the box lengths in the x, y and z directions that give the different $\alpha_{i\in\{x,y,z\}}$. The comparison with the experimental data is reported in figure 1. The simulation data with the ABOP is overall in good agreement with the experimental values, especially above 1000 K. At lower temperatures, the thermal expansion is slightly overestimated. In the range 1300−2200 K, the experimental values reported by Slack and Bartram seem to be constant. In the ABOP, $\widetilde{\alpha}$ also has this behaviour, but for the range 1000−2000 K. Above 2000 K, the lengths of the box exhibits large changes that lead to a quick increase of the thermal expansion.

In the simulation, the values of α_x and α_y are the same, except at high temperatures. Indeed, wurtzite has hexagonal symmetry, and consequently the x and y directions are not symmetrically equivalent. There is also a clear anisotropy in the thermal expansion in the z direction compared to the two other directions, which is expected for a wurtzite structure.

Figure 2 shows the phonon dispersion of the wurtzite BeO phase obtained with the ABOP and compared to DFT and experimental results [50]. Our DFT results are in good agreement with the experimental measurements. The lower acoustic branches are well reproduced in the ABOP. The subtle differences in the energies of the acoustic branches between the ABOP, DFT, and experiment are likely due to the corresponding differences in elastic constants, as seen in table 1. However, the optical branches at around 90 meV in DFT and experiments are strongly overestimated in the ABOP, with the corresponding branches at around 140−150 meV energies. The overestimation of the optical branches can be attributed to the lack of long-range

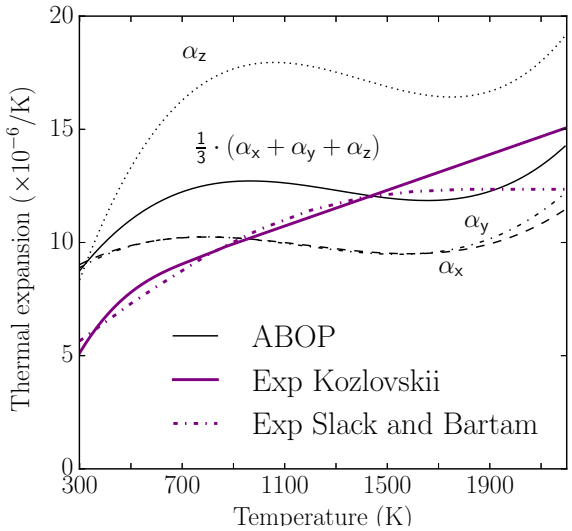

Figure 1: Thermal expansion coefficients, $\alpha_{i\in\{x,y,z\}}$, obtained from the variation of the simulation box lengths, and the directionally averaged coefficient $\widetilde{\alpha} = 1/3(\alpha_x+\alpha_y+\alpha_z)$ compared with experimental data [60, 61].

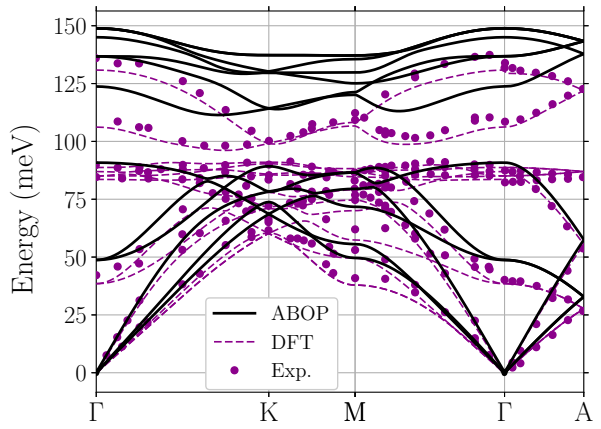

Figure 2: Phonon dispersion of wurtzite BeO calculated with the ABOP and compared with DFT calculations and experimental data from Ref. [50].

coulombic interactions in the ABOP [62], and was previously also observed in the ZnO ABOP [29].

3.2.2. Be–O molecules. Table 3 shows the bond lengths and cohesive energies of a few selected Be–O molecules predicted by the ABOP and compared with our DFT calculations and experimental results [63]. The properties of the dimer BeO are directly determined by the potential parameters D_0 and r_0. As discussed earlier, choosing D_0 to reproduce the experimental or DFT dimer energy is not compatible with the cohesive energies of the bulk BeO phases, and the bond energy of the Be–O dimer is therefore overestimated in the ABOP. $(BeO)_n$ molecules were experimentally predicted to form closed ring-like structures [63]. $(BeO)_2$ and $(BeO)_3$ rings were therefore relaxed in DFT and with the ABOP. The relaxed shape and bond angles are different in the DFT and ABOP simulations, but the bond lengths and energies are in reasonable agreement. As the number of atoms in the molecules is increased, the energy and bond length tend towards those of an infinite BeO chain, as seen in table 3. The qualitatively good agreement between the ABOP and DFT for molecules is promising for applying the ABOP in studies of surface irradiation, where sputtering of various molecules is expected.

Table 3: Bond lengths (Å) and cohesive energies (eV/atom) of different Be–O molecules predicted by the ABOP and compared with DFT results and experimental data [63].

	DFT	Exp. [63]	ABOP
BeO			
r_b	1.422		1.410
E_{coh}	−1.936	−2.3	−3.391
$(BeO)_2$			
r_b	1.555		1.617
E_{coh}	−3.631	−4.0	−3.809
$(BeO)_3$			
r_b	1.521		1.532
E_{coh}	−4.314	−4.7	−4.747
$(BeO)_\infty$ infinite chain			
r_b	1.480		1.517
E_{coh}	−4.694		−4.754

3.2.3. Interstitial oxygen atoms in Be. Formation energies for oxygen in the common high-symmetry interstitial sites in hcp Be were calculated with the ABOP, and compared to DFT calculations. The formation energy is defined as

$$E_f = E_D - n_{Be}\mu_{Be} - n_O\mu_O, \quad (13)$$

where E_D is the total energy of the system containing the defect, and n_{Be} (n_O) the number of Be (O) atoms. The chemical potentials at 0 K are given by the cohesive energies as $\mu_{Be} = -3.624$ eV and $\mu_O = E_{O_2}/2 = -2.583$ eV in the ABOP.

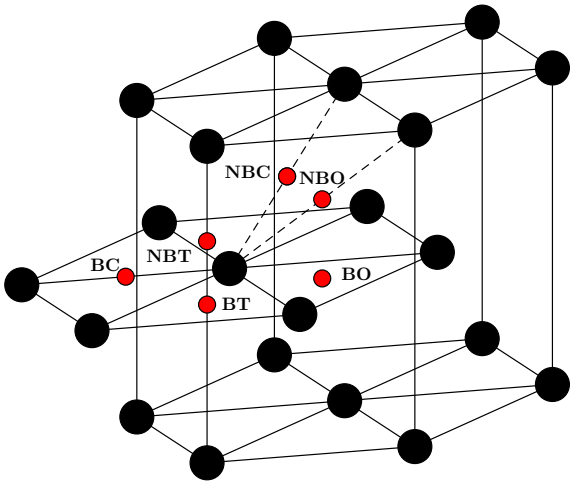

Figure 3: Common interstitial sites in the hcp lattice. BT: basal tetrahedral, BO: basal octahedral, BC: basal crowdion, NBT: non-basal tetrahedral, NBO: non-basal octahedral, and NBC: non-basal crowdion.

Table 4: Formation energies (eV) of O interstitial atoms in Be. The different interstitial sites with abbreviations are illustrated in figure 3. The values from Ref. [64] are calculated as the reported accommodation energies plus half the dissociation energy of an O_2 molecule (2.56 eV).

Site	DFT			ABOP
	This work	Ref. [64]	Ref. [65]	
BT	−0.85	−2.50	−2.37	−4.09
BO	1.82	0.21	0.39	−1.03
BC	-	-	-	−2.85
NBT	-	unstable	unstable	unstable
NBO	0.59	−1.13	−0.87	−4.06
NBC	-	-	−0.41	−2.90
r-NBT	-	-	-	−4.71

Figure 3 shows an illustration of the different interstitial sites with the adopted naming and abbreviations. The calculated formation energies are given in table 4. The most stable interstitial position according to DFT is the the basal tetrahedral (BT) site. However, as can be seen in table 4, our DFT data are about 1.5 eV higher in energy than the DFT data by Middleburgh et al. [64] and Zhang et al. [65]. On the other hand, the relative stabilities between the BT, NBO and BO interstitial sites are in good agreement (within a margin of 0.06 eV) between the three DFT studies. Thus, the reason for the difference in formation energy is clearly that the reference energy for oxygen is not the same in all three studies. To investigate the effect of the oxygen reference, we calculated the energies of oxygen atoms and molecules in different states: the spin triplet (ground state) and a state with no spin. Using the spin triplet state, we obtained the formation energies reported in table 4. However, using the state with no spin, the formation energy of O in BT becomes −2.73 eV, in NBO −1.31 eV, and in BO −0.08 eV. These values are much closer to the values reported by Zhang et al. and Middleburgh et al., indicating that their values have been calculated using a state with no spin for the oxygen reference. Clearly, no spins exist in the ABOP formalism, and the only possible reference state of oxygen is the cohesive energy of the O_2 molecule given by the ABOP parametrisation.

In the ABOP, the most stable site is a position above the BT site, close to the NBT site (denoted r-NBT in table 4). However, an oxygen interstitial at the NBT site relaxes to the BT site, as opposed to the close-by ground state r-NBT position, in agreement with DFT observations [64, 65]. The order of stability for the remaining interstitial sites predicted by the ABOP is in agreement with DFT results, although the differences in energy vary, and e.g. the stability of the NBO site is strongly overestimated.

Despite predicting the incorrect ground state oxygen interstitial site, the ABOP still qualitatively reproduces the diffusive properties obtained by DFT. The energy barrier for migration between adjacent BT sites, through an intermediate NBO site, is about 1.6 eV according to DFT calculations by Zhang et al. [65]. Although the lowest energy migration path in the ABOP is between the predicted ground state (r-NBT) and the close-by BT site along the [0001] axis (see figure 3), further migration through the bulk requires exiting the tetrahedral surrounding, following paths similar to those studied earlier in DFT. The migration energy of the BT−NBO−BT path is about 2.3 eV in the ABOP, higher than the 1.6 eV obtained by DFT [65]. In comparison, the vacancy migration in Be is about 1.3 eV in the ABOP, also higher than the DFT value of 0.72 eV reported in [64]. The self-interstitial migration energy in Be is 0.73 eV according to the ABOP [28], compared to 0.64 eV given by DFT [64]. Due to the relatively high O migration energy and the fact that the ABOP correctly predicts the O interstitial to be trapped in a tetrahedral atomic environment, even though the exact position inside the tetrahedron contradicts DFT results, can therefore be considered acceptable for most practical use in atomistic simulations. Oxygen is essentially immobile during MD time scales, which is important for oxidation and deposition simulations. Oxidation of Be surfaces is experimentally known to be limited by Be atoms migrating up through the oxide layer [66], as opposed to oxygen migrating into the Be bulk, which

due to the high oxygen migration barriers is likely to be reproduced by the ABOP. We will return to this discussion in section 3.3.1, where we study oxide layer formation and growth using the ABOP.

3.2.4. Adatom energetics on Be. Additionally, we calculated adsorption energies of oxygen atoms on a Be (0001) surface with the ABOP, and compared to DFT calculations. The adsorption energy of a single oxygen atom is defined as

$$E_{\mathrm{ad}} = E_{\mathrm{D}} - E_{\mathrm{S}} - \mu_{\mathrm{O}}, \tag{14}$$

where E_{D} is the total energy of the surface slab with the adsorbate, E_{S} the total energy of the clean surface slab, and μ_{O} the chemical potential of oxygen (-2.583 eV in the ABOP).

Figure 4 shows the common adsorption sites on a hcp (0001) surface. The corresponding adsorption energies and the distances to the surface layer are given in table 5. There is a noticeable difference in the formation energies between DFT and the ABOP. However, due to the different possibilities of treating μ_{O} in DFT, as discussed earlier, emphasis should be put on the order of stability when comparing the ABOP with DFT, and not the absolute values. The relaxed distances from the surface layer are in good agreement between DFT and the ABOP, except for the fcc site. The hcp and fcc sites have identical nearest-neighbour symmetry, and therefore similar adsorption energies. However, the ABOP predicts the fcc site as the preferred adsorption site over the hcp, in contrast to the DFT results. This is a consequence of the interaction range of the ABOP and cannot be corrected without sacrificing the fitted bulk BeO properties. For the hcp site, the second-nearest Be neighbour (the atom directly below the hcp site in the first sub-surface layer) is barely within the cutoff radius of the ABOP after relaxation, while the same atom is outside of the cutoff sphere for the fcc site. This is also evident from the difference in the relaxed distances from the surface given in table 5. The functional form of the ABOP leads to a weakening of the nearest neighbour bonds due to the second nearest neighbour for the hcp site, resulting in a higher energy than for the fcc site.

3.2.5. Point defects in BeO. The chemical potentials of the elements can vary depending on the chemical environment. The formation energy for a neutral point defect can then be expressed in the more general form used in Ref. [67], as

$$\begin{aligned} E_{\mathrm{f}} = & E_{\mathrm{D}} - \frac{1}{2}(n_{\mathrm{Be}} + n_{\mathrm{O}})\mu_{\mathrm{BeO}} \\ & - \frac{1}{2}(n_{\mathrm{Be}} - n_{\mathrm{O}})(\mu_{\mathrm{Be}} - \mu_{\mathrm{O}}) - \frac{1}{2}(n_{\mathrm{Be}} - n_{\mathrm{O}})\Delta\mu, \end{aligned} \tag{15}$$

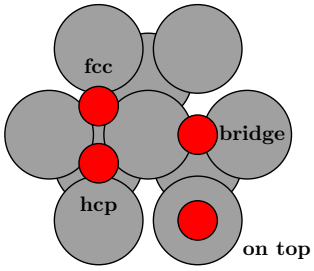

Figure 4: Adsorption sites on a hcp (0001) surface.

Table 5: Adsorption energies and relaxed distances from the surface layer for O atoms on a Be (0001) surface. See figure 4 for the positions of the different sites.

	DFT		ABOP	
Site	E_{ad} (eV)	d (Å)	E_{ad} (eV)	d (Å)
fcc	-3.10	0.91	-6.22	0.59
hcp	-3.54	0.82	-5.91	0.85
bridge	unstable		-4.72	0.71
on top	-0.74	1.52	-2.11	1.47

where $\Delta\mu$ is thermodynamically restricted to the range $-\Delta H_{\mathrm{f}} < \Delta\mu < \Delta H_{\mathrm{f}}$, and ΔH_{f} is the enthalpy of formation of BeO in its ground state phase (-4.91 eV/f.u. in the ABOP). The limits of $\Delta\mu$ correspond to O-rich and Be-rich conditions. Here, we use $\Delta\mu = 0$ in all calculations.

Formation energies of simple neutral point defects were calculated with DFT and compared to values predicted by the ABOP, as listed in table 6. The formation energies for single vacancies in BeO are strongly underestimated in the ABOP, particularly the Be vacancy. The stability of point defects in metal oxides, such as BeO or ZnO, are generally dependent on the electronic structure and charge state of the point defect [68, 69, 70], effects that the ABOP cannot capture. Good accuracy in describing point defects in BeO can therefore not be expected from the ABOP. In the case of the Be vacancy, our DFT calculation predicts a magnetisation of 2.2 μ_{B}/cell induced by the Be vacancy, which could explain the large difference in the value obtained with the ABOP. Similarly, the Be antisite induces a 2.05 μ_{B}/cell magnetisation, and consequently the difference in the formation energy predicted by the ABOP and DFT is large (around 5 eV for both the Be vacancy and antisite). Interestingly, the same 2–3 eV difference as for the O interstitial formation energies in pure Be (table 4), is observed between DFT and the ABOP for defects in BeO with an excess of one O atom (O antisite and O vacancy).

In all of these cases, DFT gives higher formation energies than the ABOP. This difference could be due to the different manner the O_2 molecule is considered, inducing a shift between the DFT and ABOP values, as discussed previously.

The lowest energy Be and O interstitial sites in BeO predicted by the ABOP were identified by creating 200 BeO systems with a randomly placed O or Be interstitial. All systems were relaxed at 1000 K and subsequently quenched to 0 K, allowing the interstitials to find a nearby energy minimum. The ground state O interstitial configuration in the ABOP (E_f = 6.75 eV) was an oxygen atom in an octahedral site on the Be-basal plane, but with strong relaxation of the geometry of the surrounding atoms. This complex configuration is likely an artefact of the potential. However, only 4 out of the 200 random simulations ended in this configuration. The majority of cases produced an O−O dumbbell with E_f = 8.08 eV or E_f = 8.57 eV, depending on the orientation. The formation energy obtained by DFT for an O interstitial in a Be-basal octahedral, corresponding to the closest high-symmetry site to the ABOP ground state configuration, is 9.50 eV. The O−O dumbbell interstitial was found to be significantly more stable in DFT, with E_f = 6.00 eV.

For the Be interstitial, the ABOP predicts a slightly off-plane O-basal octahedral site as the preferred interstitial position, with E_f = 7.50 eV. The corresponding DFT calculation resulted in relaxation of the Be atom in the opposite direction, with a final formation energy of 9.72 eV. The second lowest energy site in ABOP was an off-axis tetrahedral site with a slightly higher formation energy of 7.73 eV.

Note that only values for the lowest energy sites are listed in table 6, and in the case of an O interstitial, the DFT and ABOP values do not correspond to the same interstitial configuration. Furthermore, while the preferred sites in the ABOP certainly correspond to the global minimum energy sites for interstitials, that is not necessarily true for the DFT values, as we only considered a few selected sites. The calculated DFT values only allow a qualitative justification of the magnitudes of interstitial formation energies in BeO predicted by the ABOP.

Table 6: Formation energies (eV) of point defects in BeO. The Be vacancy and antisite both lead to a magnetisation of the cell in DFT, as indicated below the table.

	DFT	ABOP
V_O	4.42	1.62
V_{Be}	5.47[a]	0.55
O_{Be}	9.57	11.64
Be_O	12.93[b]	7.34
O_i	6.00	6.75
Be_i	9.72	7.50

[a] $M = 2.2\ \mu_B$/cell
[b] $M = 2.05\ \mu_B$/cell

3.3. Applications

3.3.1. Oxygen irradiation of Be. As an application of the Be–O ABOP, we studied the oxidation of beryllium by incident oxygen ions. Simulations of O ion irradiation at normal incidence on a (0001) Be surface were carried out. The simulations were performed using an initial cell containing 4704 atoms. The energies of the ions were 1, 10, and 100 eV, and the temperature of the Be target was 300 K, 1000 K, and 1500 K. One thousand cumulative simulations at a flux of 2.6×10^{28} m^{-2}s^{-1} were done for all energies and temperatures. Between every single bombardment, the cell was randomly shifted in the x and y directions in order to model a uniform distribution of the ions on the surface. Periodic boundaries were used in the x and y directions. The temperature of the simulation box was kept constant by controlling the temperature of the borders of the simulation cell. The two bottom layers were kept frozen to mimic an infinite lattice. 5 ps separated each bombardment. In ITER, the incident flux of plasma particles on the Be first wall is estimated to be about $10^{19}-10^{21}$ m^{-2}s^{-1} [71]. Assuming a high 10% O concentration in the plasma, one could expect an oxygen flux of around $10^{18}-10^{20}$ m^{-2}s^{-1} on the Be plasma-facing components. This is obviously a value much lower than the one used in the MD simulations, but given the short time scale available, this problem would only be resolved by increasing the surface by 10 orders of magnitude, which is not realistic at the MD length scale.

Snapshots of the irradiated (0001) Be surfaces at 300 K are shown in figure 5a-c. In the early stage of the irradiation, after around 10−100 deposited ions, the deposition region is still almost hexagonal Be. In the 100 eV irradiation case, the O atoms mainly stop in the r-NBT and NBO sites, which are the most stables sites according to the ABOP (table 4). In the lower energy cases, and especially in the 1 eV case, the ions do not have enough energy to overcome the energy barrier at the surface, and consequently remain on the surface mainly in the hcp and fcc hollow sites (table 5). After 1000 O ions, the region where the O ions stop is no longer a hexagonal Be structure, and an amorphous oxidised layer with a rough surface has been formed, as seen in figure 5. The thickness of the oxide layer decrease as the energy of the O ions decrease. For 100 eV ions, a large amount of O ions

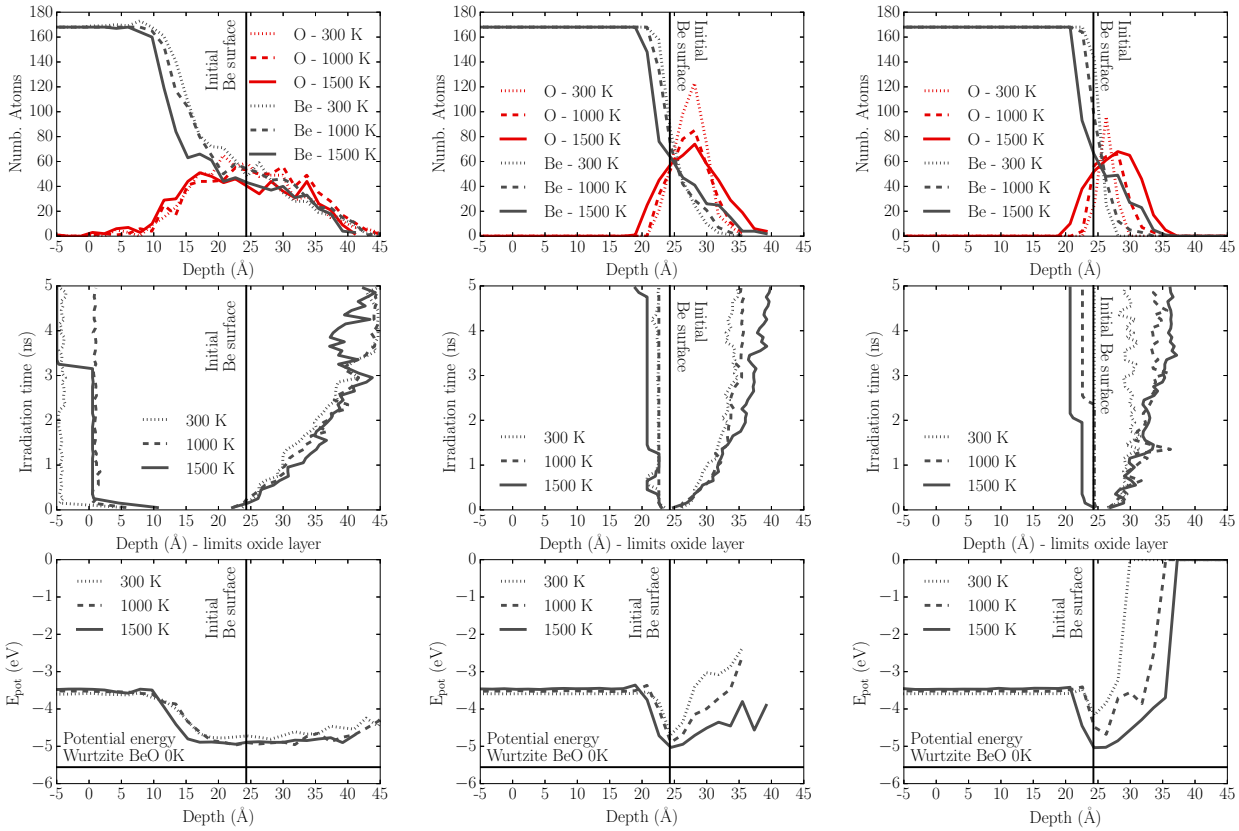

(a) 100 eV. (b) 10 eV. (c) 1 eV.

Figure 6: Profiles of O and Be atoms (upper figures), time evolution of the limits of the oxide layer (middle figures), and potential energy per atom (lower figures) as functions of depth, after bombardment of 1000 O ions on a (0001) Be with energies 100 eV (a), 10 eV (b), and 1 eV (c). The initial position of the (0001) surface is indicated by the black vertical lines, and the black horizontal lines correspond to the potential energy of the perfect wurtzite BeO structure. In some cases, particles have been sputtered during the 1000th irradiation, and are not taken into account in the plots. In these cases, the potential energy goes to 0 eV (and marks the position of the surface of the oxide layer).

are implanted below the surface while for 1 eV ions, the O ions are almost exclusively stuck on top of the surface. The roughness of the oxide surface is most pronounced for the irradiation with 100 eV ions. These ions have enough energy to cause sputtering from the surface, and also induce damage deep below the surface (figure 5a). For 100 eV ions at 300 K, several O atoms are also seen much deeper than the oxidised layer. These deep atoms are results of channelling [72], where ions travel through the material in lines of low atomic density. Channelled ions are also observed in the irradiations at 1000 K and 1500 K, but closer to the surface. This could be explained by the increased thermal motion of the target atoms at the higher temperatures, effectively making the channelling paths more narrow.

To further analyse the process of oxidation in our MD simulations, atom profiles (Be and O), time evolutions of the limits of the oxide layer as well as potential energy per atom profiles were plotted as functions of depth. The limits of the oxide layer are constructed by looking at the depth of the deepest oxygen atom and the one closest to the vacuum limit. Thus, in the 100 eV case, channelled ions might be taken into account. These plots are presented in figure 6a-c for the three temperatures and the three energies. The initial position of the (0001) Be surface is indicated with a vertical line, in order to see where the oxidised layer is formed. The oxide layer and its growth can be divided into two zones: the one below the initial surface and the one above the initial surface. To explain the growth of the oxide layer toward the bulk, one could propose either implantation of O ions or diffusion of O through Be. Similarly, to explain the growth toward the vacuum, migration of Be through the oxide layer could be envisaged, which can be caused

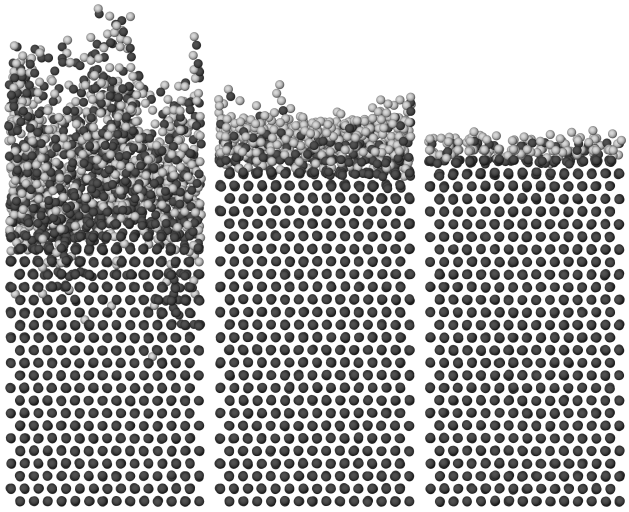

(a) 100 eV. (b) 10 eV. (c) 1 eV.

Figure 5: Snapshots of the beryllium surfaces bombarded at 300 K by 1000 O ions with energies 100 eV (a), 10 eV (b), and 1 eV (c). The grey circles correspond to beryllium atoms and white circles to oxygen atoms.

either by transfer of recoil energy or diffusion of Be through the layer. The latter process has been used to explain the growth mechanism of oxide layers in experiments by Roth et al. [66, 6]. The following analyses of figure 6 is an attempt to discriminate which of these mechanisms limits the growth rate of the oxide layer.

For 100 eV ions (figure 6a), the oxide layer has a thickness of about 35 Å at all temperatures (excluding the channelled ions). The layer is equivalently distributed below and above the initial Be surface. This evidences the fact that part of the oxidised layer is formed by implantation of the O ions. However, as can be seen in the Be profiles, some Be atoms are also extracted from below the surface to construct a sparse oxide layer above the initial Be surface. Looking at the time evolution of the oxide layer limit below the initial Be surface, one can see straight lines at the same depth for all temperatures within an approximation of a few Å. This depth corresponds to the maximum implantation depth of the O ions, meaning that the growth of the oxide layer toward the bulk is mainly due to implantation of the ions. On the other hand, the limit of the oxide layers above the initial Be surface keeps growing as the implantation time increases. For the three temperatures considered, the growth is almost identical (within a margin of a few Å), indicating that the limiting process does not seem to be temperature-dependent. Thus, diffusion of Be atoms is unlikely to be the limiting oxidation mechanism for 100 eV ions, instead the transfer of kinetic energy from the O ions to the Be atoms seems to be the main growth mechanism. Looking at the profiles of potential energy per atom, one can see that in the oxidised region, the potential energy drops from about −3.5 eV (pure Be) to a minimum of −5.0 eV. The minimum potential energy is obtained for a O/Be ratio of 1, meaning that stoichiometric BeO is preferentially formed in the oxide layer. However, the potential energy does not reach that of perfect wurtzite (horizontal line in the lower plots) even after cooling of the oxidised structure to 0 K. The time scale for formation of a crystalline wurtzite BeO layer is likely beyond reach for MD, and the oxide layer is still in an amorphous BeO phase (see figure 5a).

For 10 eV ions (figure 6b), the oxide layer has a thickness between 11.0 Å (300 K), and 20.2 Å (1500 K), i.e. an increase in thickness of about 80%. Unlike the 100 eV case, most of the oxidised layer is above the initial Be surface, and only a few atoms are implanted below the surface. As previously mentioned, the limit of the oxide layer below the initial Be surface is almost a straight line at the maximum depth of implantation of the ions, with no clear time evolution toward the bulk or the surface. On the other hand, the limit of the layer above the initial surface keeps growing with time. In addition, a clear temperature effect can be seen that explains the thickness increase between 300 K and 1500 K. In this case, the limiting growth mechanism is a thermally activated process, i.e. the diffusion mechanism of oxide layer growth seem to be significant even at MD time scales for this range of small thicknesses. The effect of temperature is also clearly seen in the potential energy profile in figure 6b. The oxide layer formed at a high temperature is more stable by 0.34 eV/atom, bringing the oxide layer closer to a wurtzite configuration (in terms of potential energy). Again, the minimum potential energy is obtained for a O/Be ratio of 1 at all temperatures.

The observations discussed above for the 10 eV ions are also true for the 1 eV case (figure 6c), but now even more pronounced. At 300 K, the resulting layer after 1000 bombardments can hardly be called an oxide layer, and is essentially a complete layer of adsorbed O atoms on top of the Be surface: the lower limit of the oxide layer almost overlaps with the position of the initial surface, indicating no implantation. The thickness of the layer is only 3.7 Å, which is less than the lattice constant of the wurtzite in the [0001] direction (table 1). In addition, the upper limit of the layer stays constant after about 2 ns (400 incident O ions) and the total number of adsorbed atoms stays approximately equal to 130 O atoms. Consequently, the decrease in the potential energy at 300 K is only 0.59 eV in the O-adsorbed layer compared to the pure Be bulk. At 1000 K and 1500 K, the situation is completely different. The thickness of the

oxide layer is significantly increased, and is 14.7 Å at 1500 K, which is comparable to the thickness of the oxide layer for the 10 eV irradiation at the same temperature, and represents an increase in thickness of about 300%. Looking at the limits of the oxide layer, one can conclude that this increase occurs mainly above the initial surface with a clear temperature dependence. In addition, as in the case of the 10 eV irradiation, the potential energy of the oxide layer decreases substantially as the temperature is increased. The oxide layer at 1500 K is 0.84 eV/atom more stable than the layer at 300 K. Thus, the strong temperature dependence even at a very low energy of the incident ions suggests that a thermally activated process, such as diffusion of atoms through the oxide layer, is the origin of the growth of the oxide layer at higher temperatures, as proposed by Roth et al. [73, 66, 6]

To summarise the observations, at 100 eV, no clear temperature effect is observed. Thus, the thickness of the oxide layer is mostly controlled by the implantation of O ions (toward the bulk of the material) and the migration of Be due to energy transfer from the incident O ions to the Be atoms. Below 10 eV, the growth of the oxide layer is thermally activated and mainly directed toward the vacuum. It suggests that the diffusion of Be atoms through the oxide layer is the limiting process, which is in line with experimental observations [73, 66, 6]. Here, it is worth noting that the oxidation toward the substrate might be underestimated due to the overestimation of the energy barrier for O migration in Be. To quantify this possible underestimation, we can use the Wert and Zener theory [74] to estimate the pre-exponential factor of the diffusion coefficient of O in Be (in our cases ranging around $5{-}6{\times}10^{-7}$ $\mathrm{m^2 s^{-1}}$). Thus, assuming the characteristic diffusion length l_{diff} is estimated as $l_{\mathrm{diff}} = \sqrt{D_{\mathrm{O}} t}$ (where D_{O} is the diffusion coefficient of O in Be), the diffusion length in these MD simulations can be estimated for both the 1.6 eV (DFT) and the 2.3 eV (ABOP) migration barriers. For the 1500 K case, where the highest migration depth can be expected, one obtains $l_{\mathrm{diff}}^{\mathrm{DFT}} \approx 1$ Å and $l_{\mathrm{diff}}^{\mathrm{ABOP}} \approx 2$ pm. In both cases, the characteristic length of migration is much smaller than the resulting thickness of the formed oxide layer. Thus, oxygen migration into the Be bulk does not affect the growth rate of the oxide layer, and cannot be the rate-limiting growth mechanism, despite the overestimation of the migration energy in the ABOP.

Finally, the irradiation simulations allow us to investigate the sputtering of beryllium by oxygen ions at different temperatures and incident energies. Figure 7 shows the evolution of the sputtering yields (number of sputtered Be atoms per incoming O ions) as a function of incident O energy for the three different temperatures used in the simulations. In addition to the sputtering yields obtained by the MD simulations, SRIM [75] simulations are completed to compare the MD results to results obtained in the binary collision approximation (BCA). For these calculations, we used SRIM version 2013.00 in the Monolayer collision steps/Surface sputtering mode, with a density of 3.01 g/cm^3 and default values for the other parameters. These were the displacement energy of 25 eV for Be and 28 eV for O in BeO, lattice binding energy of 3 eV for both elements, and surface binding energies of 3.38 eV for Be and 2 eV for O. For each energy, 100 000 incoming O ions were simulated.

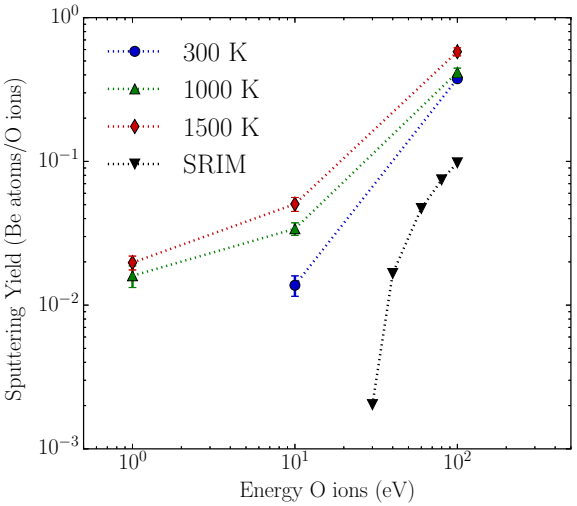

Figure 7: Sputtering yields of Be by O ions at different temperatures and energies. The MD data are compared to the sputtering yield given by BCA using SRIM [75]. The error bars are the standard errors obtained after repeating the 1000 O irradiation series four times for each temperature and energy.

The SRIM simulations only give non-zero sputtering yields for incident energies above 30 eV. In addition, the sputtering yield calculated by SRIM is underestimated by one order of magnitude compared to the MD-calculated values. This large discrepancy is explained by the strong chemical sputtering of Be by O ions. Chemical sputtering is dominant in the range of ion energies and temperatures considered here. At 1 eV and 10 eV, the sputtering yield is even purely chemical. Thus, from these simulations, it is clear that to accurately tackle the issue of beryllium sputtering by oxygen ions in tokamaks, MD is needed. The products of the chemical sputtering are mainly BeO and BeO_2, even though a few larger molecules like Be_2O_3 or Be_3O_4 are eventually observed once a O/Be ratio of 1 is obtained in the oxidised layer. The chemical erosion for 100 eV irradiation is found to be dependent on the state of the oxidised layer. In the first stage of the

irradiation, only single Be atoms are eroded from the surface, but once the oxidised layer has a O/Be ratio of about 1, molecules are eventually sputtered. From figure 7, it is also clear that the erosion is much more pronounced at higher energies, and that the temperature, by increasing the motion of the beryllium atoms on the surface, increases sputtering from the surface. Thus, for 1 eV irradiation, no sputtering is observed at 300 K while at 1000 K and 1500 K, significant erosion of the material is observed.

3.3.2. Thermal stability and elasticity of BeO nanosheets and nanotubes. We applied the Be–O ABOP in an investigation of the thermal stability and elasticity of BeO nanosheets and nanotubes. Carbon graphene has been shown to be thermally very stable with an estimated melting point of around 4500 K [76]. To estimate the melting point of the corresponding BeO sheet with the ABOP, we carried out MD simulations with different heating rates. The system consisted of 800 atoms with periodic boundaries in the planar dimensions. The BeO sheet was heated up at zero pressure with three different heating rates, 10 K/ps, 5 K/ps, and 2.5 K/ps. The observed melting point was about 3300 K and did not significantly change with the different heating rates. More sophisticated methods have been used to obtain more accurate estimates of the melting point of (carbon) graphene [76], but this is beyond the scope of this work. The obtained melting point of 3300 K should therefore be considered an upper limit predicted by the ABOP.

Snapshots from the melting simulation are seen in figure 8. During high temperatures, breaking of individual Be–O bonds was common, with neighbouring Be and O atoms moving in opposite out-of-plane directions. However, individual bond breaking rarely resulted in any permanent damage, as the bond was generally reformed quickly. At temperatures close to the observed melting point, bond breaking often lead to chains or entire hexagons of BeO being temporarily detached from the nanosheet, connected only by chains of Be and O atoms as seen in figure 8a. Figure 8b shows the onset of the melting process, where the first permanently damaged regions are formed. Melting occurred by the entire nanosheet separating into chain- and ring-like BeO structures with two- and three-fold coordinations, as seen in figure 8c.

The stability of the BeO nanosheet close to the observed melting point was assessed in a constant temperature simulation at 3000 K. Previously, Wu et al. [15] studied the thermal stability of a BeO nanoribbon with ab initio MD, and observed that the nanoribbon remained intact throughout a 5 ps simulation at 2000 K. Using the ABOP, we can extend the time scale to nanoseconds. The BeO sheet remained stable throughout the 1 ns simulation time, altough two BeO molecules were released, leaving vacancies in the monolayer.

The elasticity of nanotubes predicted by the ABOP was compared with published DFT results of the Young's modulus. The Young's modulus for 3D structures is typically calculated as the second derivative of the energy with respect to the strain at equilibrium, divided by the equilibrium volume. Due to the ambiguity of defining the shell thickness when calculating the volume of a nanotube, the Young's modulus for nanotubes is conventionally defined [77] using the equilibrium area of the cylindrical nanotube shell S_0, as

$$Y = \frac{1}{S_0}\frac{\partial^2 E}{\partial \varepsilon^2}\bigg|_{\varepsilon=0}, \tag{16}$$

where $S_0 = 2\pi LR$, L is the length, and R is the radius of the nanotube. Baumeier et al. [11] calculated the Young's moduli for both armchair, expressed by chiral indices (n, n), and zigzag, $(n, 0)$, BeO nanotubes as a function of the diameter. The corresponding Young's moduli for both armchair and zigzag nanotubes were calculated using the ABOP. The length of the nanotubes was about 50 Å, and periodic boundaries were used in the length dimension. The potential energy as a function of strain at 0 K was extracted by statically straining the nanotube around the equilibrium length, and carrying out conjugate gradient energy minimisations at each strain value. The Young's modulus was then obtained from a second order polynomial fit to the strain–energy curve according to equation 16.

Figure 9 shows the Young's modulus as a function of diameter calculated with the ABOP and compared to DFT results by Baumeier et al. [11]. The ABOP slightly overestimates the Young's moduli compared to the DFT data, but the overall trend is similar. The zigzag type nanotubes are elastically softer than the armchair nanotubes, and the Young's modulus rapidly tends towards the value of the infinite graphene-like sheet, in agreement with DFT. Recently, Baima et al. [12] also calculated the Young's modulus of zigzag BeO nanotubes in DFT, and obtained values slightly higher than the results of Baumeier et al. given in figure 9. The calculated Young's modulus of the infinite nanosheet with the ABOP is 0.163 TPa nm, compared to the DFT values 0.13 TPa nm by Baumeier et al., and 0.137 TPa nm by Baima et al.

Finally, we used the ABOP to estimate the temperature-dependence of the Young's modulus of BeO nanotubes. Figure 10 shows the obtained data for an armchair (7, 7) and a zigzag (12, 0) nanotube. The Young's moduli were calculated from a linear fit to the stress-strain response of the stepwise strained

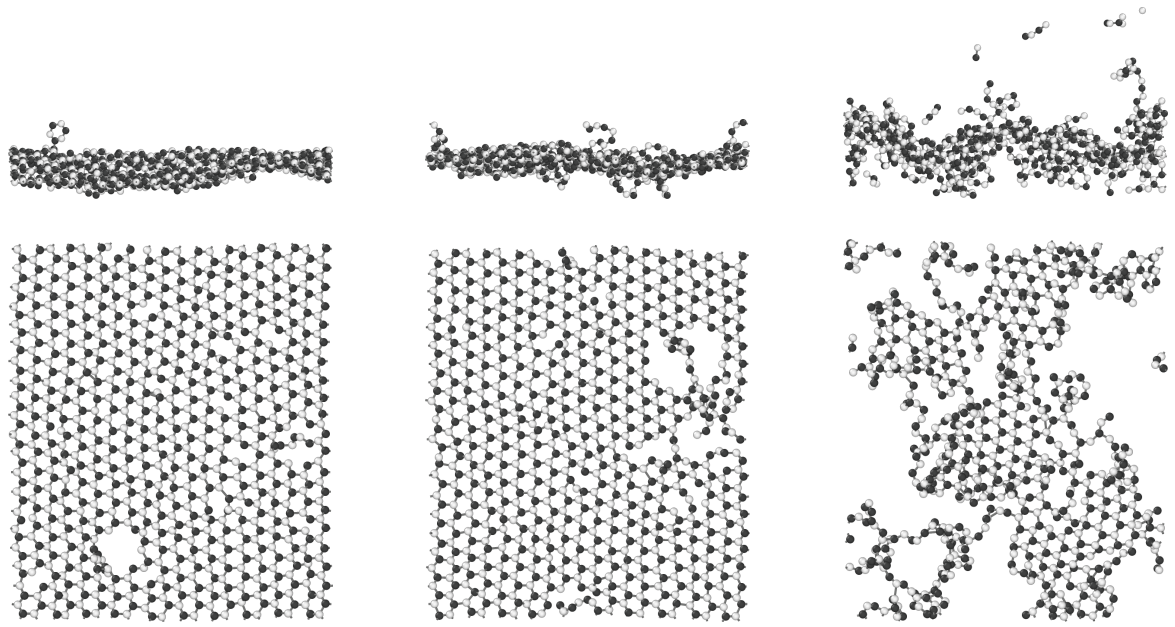

(a) 3200 K, 1.282 ns. (b) 3280 K, 1.316 ns. (c) 3310 K, 1.333 ns.

Figure 8: Snapshots (side and top views) of the melting of a BeO nanosheet simulated with the ABOP. Be atoms are coloured grey and O atoms white.

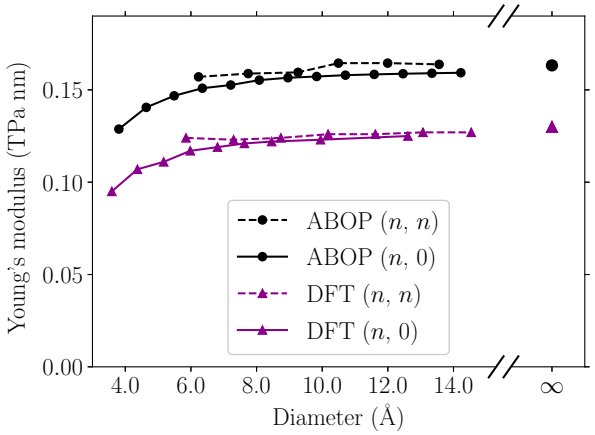

Figure 9: Young's modulus of armchair (n, n) and zigzag $(n, 0)$ BeO nanotubes as a function of the diameter, calculated with the ABOP and compared with DFT results [11]. The limiting values for the infinite graphene-like BeO sheet are given at the right.

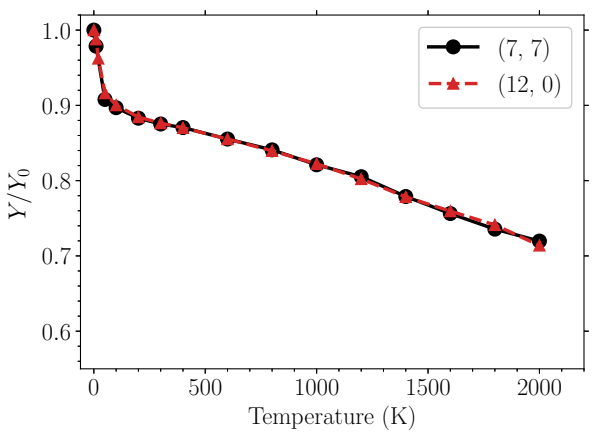

Figure 10: Young's modulus as a function of temperature, normalised by the 0 K value, as predicted by the ABOP for both armchair (7, 7) and zigzag (12, 0) BeO nanotubes.

nanotube, which proved to be more accurate than using the potential energy at high temperatures. Each data point in figure 10 is an average of three simulations. The armchair and zigzag nanotubes show identical elastic softening as a function of temperature, and since the Young's modulus for both types quickly becomes independent of diameters (figure 9), a similar behaviour can also be expected for BeO nanotubes of any size. Figure 10 shows that the Young's modulus drops rapidly in the 0−100 K range, after which the it decreases linearly to about 73% of the 0 K value at 2000 K. A rapid drop in the Young's modulus has previously been observed for carbon nanotubes at around 1100 K [78], similar to the low-temperature behaviour observed here, and was hypothesised to be due to the onset of a subtle change in the atomic structure. In our simulations, however, no clear

structural changes could be identified. Nevertheless, in reality, zero-point vibrations would likely dominate over thermal vibrations at low temperatures and result in a different behaviour than predicted by MD.

4. Conclusions

An analytical bond order potential for the Be–O system was fitted and tested against a large database of density functional theory results. The potential shows promising capabilities for simulations of the fusion-relevant Be–O surface interactions. The structural, elastic, thermal, and phonon properties of BeO are well reproduced, as well as the energetics of simple Be–O molecules. Point defect and diffusion properties in Be and BeO obtained by DFT are qualitatively reproduced by the potential. The potential was applied in simulations of the early stages of oxidation of a Be surface by irradiation at different energies and temperatures. We observed the formation of an oxide layer on the Be surface and investigated the possible growth mechanisms. Additionally, we found that chemical sputtering of different Be–O molecules is significant even at very low ion energies. Finally, the potential was shown to be suited for simulations of BeO nanotubes and nanosheets. We provided an estimate of the melting point of BeO nanosheets as well as for the temperature-dependence of the Young's modulus of BeO nanotubes.

Acknowledgements

This work has been carried out within the framework of the EUROfusion Consortium and has received funding from the Euratom research and training programme 2014-2018 under grant agreement No 633053. The views and opinions expressed herein do not necessarily reflect those of the European Commission. The authors of this work were granted access to the HPC resources of IDRIS and CINES under the allocation A0020806612 made by GENCI (Grand Equipement National de Calcul Intensif) and to the Marconi Supercomputer at CINECA SuperComputing Application and Innovation Department, Bologna, Italy. Grants of computer capacity from CSC - IT Center for Science, Finland are gratefully acknowledged. JB acknowledges financial support from Svenska Kulturfonden (Arvid och Greta Olins fond).

References

[1] Federici G 2006 *Physica Scripta* **2006** 1 ISSN 1402-4896 URL http://stacks.iop.org/1402-4896/2006/i=T124/a=001

[2] Brezinsek S, Stamp M F, Nishijima D, Borodin D, Devaux S, Krieger K, Marsen S, O'Mullane M, C Bjoerkas, Kirschner A and contributors J E 2014 *Nuclear Fusion* **54** 103001 ISSN 0029-5515 URL http://stacks.iop.org/0029-5515/54/i=10/a=103001

[3] Nordlund K, Björkas C, Ahlgren T, Lasa A and Sand A E 2014 *Journal of Physics D: Applied Physics* **47** 224018 ISSN 0022-3727 URL http://stacks.iop.org/0022-3727/47/i=22/a=224018

[4] Björkas C, Borodin D, Kirschner A, Janev R K, Nishijima D, Doerner R and Nordlund K 2013 *Plasma Physics and Controlled Fusion* **55** 074004 ISSN 0741-3335 URL http://stacks.iop.org/0741-3335/55/i=7/a=074004

[5] Safi E, Valles G, Lasa A and Nordlund K 2017 *Journal of Physics D: Applied Physics* **50** 204003 ISSN 0022-3727 URL http://stacks.iop.org/0022-3727/50/i=20/a=204003

[6] Roth J, Doerner R, Baldwin M, Dittmar T, Xu H, Sugiyama K, Reinelt M, Linsmeier C and Oberkofler M 2013 *Journal of Nuclear Materials* **438, Supplement** S1044–S1047 ISSN 0022-3115 URL http://www.sciencedirect.com/science/article/pii/S0022311513002365

[7] Reinelt M, Allouche A, Oberkofler M and Linsmeier C 2009 *New Journal of Physics* **11** 043023 ISSN 1367-2630 URL http://stacks.iop.org/1367-2630/11/i=4/a=043023

[8] Ivanovskii A L 2012 *Russian Chemical Reviews* **81** 571 ISSN 0036-021X URL http://iopscience.iop.org/article/10.1070/RC2012v081n07ABEH004302/meta

[9] Tang Q and Zhou Z 2013 *Progress in Materials Science* **58** 1244–1315 ISSN 0079-6425 URL http://www.sciencedirect.com/science/article/pii/S0079642513000376

[10] Sorokin P B, Fedorov A S and Chernozatonskii L A 2006 *Physics of the Solid State* **48** 398–401 ISSN 1063-7834, 1090-6460 URL https://link.springer.com/article/10.1134/S106378340602034X

[11] Baumeier B, Krüger P and Pollmann J 2007 *Physical Review B* **76** 085407 URL https://link.aps.org/doi/10.1103/PhysRevB.76.085407

[12] Baima J, Erba A, Rérat M, Orlando R and Dovesi R 2013 *The Journal of Physical Chemistry C* **117** 12864–12872 ISSN 1932-7447 URL http://dx.doi.org/10.1021/jp402340z

[13] Gorbunova M A, Shein I R, Makurin Y N, Ivanovskaya V V, Kijko V S and Ivanovskii A L 2008 *Physica E: Low-dimensional Systems and Nanostructures* **41** 164–168 ISSN 1386-9477 URL http://www.sciencedirect.com/science/article/pii/S1386947708002385

[14] He J, Wu K, Sa R, Li Q and Wei Y 2010 *Applied Physics Letters* **97** 051901 ISSN 0003-6951 URL http://aip.scitation.org/doi/abs/10.1063/1.3473726

[15] Wu W, Lu P, Zhang Z and Guo W 2011 *ACS Applied Materials & Interfaces* **3** 4787–4795 ISSN 1944-8244 URL http://dx.doi.org/10.1021/am201271j

[16] Fathalian A, Moradian R and Shahrokhi M 2013 *Solid State Communications* **156** 1–7 ISSN 0038-1098 URL http://www.sciencedirect.com/science/article/pii/S003810981200645X

[17] Rastegar S F, Ahmadi Peyghan A and Soleymanabadi H 2015 *Physica E: Low-dimensional Systems and Nanostructures* **68** 22–27 ISSN 1386-9477 URL http://www.sciencedirect.com/science/article/pii/S1386947714004330

[18] Tersoff J 1986 *Physical Review Letters* **56** 632–635 URL http://link.aps.org/doi/10.1103/PhysRevLett.56.632

[19] Tersoff J 1988 *Physical Review B* **37** 6991–7000 URL http://link.aps.org/doi/10.1103/PhysRevB.37.6991

[20] Abell G C 1985 *Physical Review B* **31** 6184–6196 URL http://link.aps.org/doi/10.1103/PhysRevB.31.6184

[21] Brenner D W 1989 *Physical Review Letters* **63** 1022–1022

URL http://link.aps.org/doi/10.1103/PhysRevLett.63.1022

[22] Daw M S and Baskes M I 1984 *Physical Review B* **29** 6443–6453 URL http://link.aps.org/doi/10.1103/PhysRevB.29.6443

[23] Albe K, Nordlund K and Averback R S 2002 *Physical Review B* **65** 195124 URL http://link.aps.org/doi/10.1103/PhysRevB.65.195124

[24] Müller M, Erhart P and Albe K 2007 *Journal of Physics: Condensed Matter* **19** 326220 ISSN 0953-8984 URL http://iopscience.iop.org/0953-8984/19/32/326220

[25] Juslin N, Erhart P, Träskelin P, Nord J, Henriksson K O E, Nordlund K, Salonen E and Albe K 2005 *Journal of Applied Physics* **98** 123520 ISSN 00218979 URL http://scitation.aip.org/content/aip/journal/jap/98/12/10.1063/1.2149492

[26] Ahlgren T, Heinola K, Juslin N and Kuronen A 2010 *Journal of Applied Physics* **107** 033516 ISSN 0021-8979 URL http://aip.scitation.org/doi/abs/10.1063/1.3298466

[27] Henriksson K O E, Björkas C and Nordlund K 2013 *Journal of Physics: Condensed Matter* **25** 445401 ISSN 0953-8984 URL http://stacks.iop.org/0953-8984/25/i=44/a=445401

[28] Björkas C, Juslin N, Timko H, Vörtler K, Nordlund K, Henriksson K and Erhart P 2009 *Journal of Physics: Condensed Matter* **21** 445002 ISSN 0953-8984 URL http://stacks.iop.org/0953-8984/21/i=44/a=445002

[29] Erhart P, Juslin N, Goy O, Nordlund K, Müller R and Albe K 2006 *Journal of Physics: Condensed Matter* **18** 6585 ISSN 0953-8984 URL http://iopscience.iop.org/0953-8984/18/29/003

[30] Björkas C, Henriksson K O E, Probst M and Nordlund K 2010 *Journal of Physics: Condensed Matter* **22** 352206 ISSN 0953-8984 URL http://stacks.iop.org/0953-8984/22/i=35/a=352206

[31] Brenner D W 1990 *Physical Review B* **42** 9458–9471 URL http://link.aps.org/doi/10.1103/PhysRevB.42.9458

[32] Morse P M 1929 *Physical Review* **34** 57–64 URL http://link.aps.org/doi/10.1103/PhysRev.34.57

[33] Ziegler J F, Biersack J P and Littmarck U 1985 The Stopping and Range of Ions in Matter *Treatise on Heavy-Ion Science* (Pergamon) pp 93–129 ISBN 978-1-4615-8105-5 978-1-4615-8103-1 URL http://link.springer.com/chapter/10.1007/978-1-4615-8103-1_3

[34] Henriksson K O E 2013 TULIP: Program for fitting an interatomic potential to data

[35] Nordlund K, Ghaly M, Averback R S, Caturla M, Diaz de la Rubia T and Tarus J 1998 *Physical Review B* **57** 7556–7570 URL http://link.aps.org/doi/10.1103/PhysRevB.57.7556

[36] Ghaly M, Nordlund K and Averback R S 1999 *Philosophical Magazine A* **79** 795–820 ISSN 0141-8610 URL http://dx.doi.org/10.1080/01418619908210332

[37] Plimpton S 1995 *Journal of Computational Physics* **117** 1–19 ISSN 0021-9991 http://lammps.sandia.gov URL http://www.sciencedirect.com/science/article/pii/S002199918571039X

[38] Nordlund K 1995 *Computational Materials Science* **3** 448–456 ISSN 0927-0256 URL http://www.sciencedirect.com/science/article/pii/092702569400085Q

[39] Bahn S R and Jacobsen K W 2002 *Computing in Science Engineering* **4** 56–66 ISSN 1521-9615

[40] Giannozzi P, Baroni S, Bonini N, Calandra M, Car R, Cavazzoni C, Davide Ceresoli, Chiarotti G L, Cococcioni M, Dabo I, Corso A D, Gironcoli S d, Fabris S, Fratesi G, Gebauer R, Gerstmann U, Gougoussis C, Anton Kokalj, Lazzeri M, Martin-Samos L, Marzari N, Mauri F, Mazzarello R, Stefano Paolini, Pasquarello A, Paulatto L, Sbraccia C, Scandolo S, Sclauzero G, Seitsonen A P, Smogunov A, Umari P and Wentzcovitch R M 2009 *Journal of Physics: Condensed Matter* **21** 395502 ISSN 0953-8984 URL http://stacks.iop.org/0953-8984/21/i=39/a=395502

[41] McKeehan L W 1922 *Proceedings of the National Academy of Sciences of the United States of America* **8** 270–274 ISSN 0027-8424 URL http://www.ncbi.nlm.nih.gov/pmc/articles/PMC1085143/

[42] Aminoff G 1925 *Zeitschrift für Kristallographie - Crystalline Materials* **62** 113–122 ISSN 2196-7105 URL https://www.degruyter.com/view/j/zkri.1925.62.issue-1-6/zkri.1925.62.1.113/zkri.1925.62.1.113.xml

[43] Hazen R M and Finger L W 1986 *Journal of Applied Physics* **59** 3728–3733 ISSN 0021-8979 URL http://aip.scitation.org/doi/abs/10.1063/1.336756

[44] Sabine T M and Hogg S 1969 *Acta Crystallographica Section B: Structural Crystallography and Crystal Chemistry* **25** 2254–2256 ISSN 0567-7408 URL http://scripts.iucr.org/cgi-bin/paper?a06964

[45] Vidal-Valat G, Vidal J P, Kurki-Suonio K and Kurki-Suonio R 1987 *Acta Crystallographica Section A: Foundations of Crystallography* **43** 540–550 ISSN 0108-7673 URL http://scripts.iucr.org/cgi-bin/paper?a26524

[46] Downs J W, Ross F K and Gibbs G V 1985 *Acta Crystallographica Section B: Structural Science* **41** 425–431 ISSN 0108-7681 URL http://scripts.iucr.org/cgi-bin/paper?a24453

[47] 2015 CRC Handbook of Chemistry and Physics, 96th Edition URL https://www.crcpress.com/CRC-Handbook-of-Chemistry-and-Physics-96th-Edition/Haynes/9781482260977

[48] Bentle G G 1966 *Journal of the American Ceramic Society* **49** 125–128 ISSN 1551-2916 URL http://onlinelibrary.wiley.com/doi/10.1111/j.1151-2916.1966.tb15389.x/abstract

[49] Cline C F, Dunegan H L and Henderson G W 1967 *Journal of Applied Physics* **38** 1944–1948 ISSN 0021-8979 URL http://aip.scitation.org/doi/abs/10.1063/1.1709787

[50] Bosak A, Schmalzl K, Krisch M, van Beek W and Kolobanov V 2008 *Physical Review B* **77** 224303 URL https://link.aps.org/doi/10.1103/PhysRevB.77.224303

[51] Allouche A and Ferro Y 2015 *Solid State Ionics* **272** 91–100 ISSN 0167-2738 URL http://www.sciencedirect.com/science/article/pii/S016727381500020X

[52] Wrasse E O and Baierle R J 2012 *Physics Procedia* **28** 79–83 ISSN 1875-3892 URL http://www.sciencedirect.com/science/article/pii/S1875389212011595

[53] Shein I R, Gorbuniva M A, Makurin Y N, Kiiko V S and Ivanovskii A L 2008 *International Journal of Modern Physics B* **22** 4987–4992 ISSN 0217-9792 URL http://www.worldscientific.com/doi/abs/10.1142/S0217979208049248

[54] Perdew J P, Burke K and Ernzerhof M 1996 *Physical Review Letters* **77** 3865–3868 URL https://link.aps.org/doi/10.1103/PhysRevLett.77.3865

[55] Vanderbilt D 1990 *Physical Review B* **41** 7892–7895 URL https://link.aps.org/doi/10.1103/PhysRevB.41.7892

[56] Giannozzi P, de Gironcoli S, Pavone P and Baroni S 1991 *Physical Review B* **43** 7231–7242 URL https://link.aps.org/doi/10.1103/PhysRevB.43.7231

[57] Pauling L 1960 *The Nature of the Chemical Bond and the Structure of Molecules and Crystals: An Introduction to Modern Structural Chemistry* (Cornell University Press) ISBN 0-8014-0333-2

[58] Haas P, Tran F and Blaha P 2009 *Physical Review B* **79** 085104 URL https://link.aps.org/doi/10.1103/PhysRevB.79.085104

[59] Nordlund K and Averback R S 1998 *Physical Review Letters* **80** 4201–4204 URL https://link.aps.org/doi/10.1103/PhysRevLett.80.4201

[60] Kozlovskii Y M and Stankus S V 2014 *High Temperature* **52** 536–540 ISSN 0018-151X, 1608-3156 URL https://link.springer.com/article/10.1134/S0018151X1403016X

[61] Slack G A and Bartram S F 1975 *Journal of Applied Physics* **46** 89–98 ISSN 0021-8979, 1089-7550 URL http://aip.scitation.org/doi/10.1063/1.321373

[62] Ashcroft N W and Mermin N D 1976 *Solid State Physics* (Saunders College Publishing)

[63] Chupka W A, Berkowitz J and Giese C F 1959 *The Journal of Chemical Physics* **30** 827–834 ISSN 0021-9606 URL http://aip.scitation.org/doi/abs/10.1063/1.1730053

[64] Middleburgh S C and Grimes R W 2011 *Acta Materialia* **59** 7095–7103 ISSN 1359-6454 URL http://www.sciencedirect.com/science/article/pii/S1359645411005507

[65] Zhang P, Zhao J and Wen B 2012 *Journal of Nuclear Materials* **423** 164–169 ISSN 0022-3115 URL http://www.sciencedirect.com/science/article/pii/S0022311512000396

[66] Roth J, Wampler W R and Jacob W 1997 *Journal of Nuclear Materials* **250** 23–28 ISSN 0022-3115 URL http://www.sciencedirect.com/science/article/pii/S0022311597002365

[67] Qian G X, Martin R M and Chadi D J 1988 *Physical Review B* **38** 7649–7663 URL https://link.aps.org/doi/10.1103/PhysRevB.38.7649

[68] Kohan A F, Ceder G, Morgan D and Van de Walle C G 2000 *Physical Review B* **61** 15019–15027 URL https://link.aps.org/doi/10.1103/PhysRevB.61.15019

[69] Erhart P, Klein A and Albe K 2005 *Physical Review B* **72** 085213 URL https://link.aps.org/doi/10.1103/PhysRevB.72.085213

[70] Janotti A and Van de Walle C G 2007 *Physical Review B* **76** 165202 URL https://link.aps.org/doi/10.1103/PhysRevB.76.165202

[71] Roth J, Tsitrone E, Loarte A, Loarer T, Counsell G, Neu R, Philipps V, Brezinsek S, Lehnen M, Coad P, Grisolia C, Schmid K, Krieger K, Kallenbach A, Lipschultz B, Doerner R, Causey R, Alimov V, Shu W, Ogorodnikova O, Kirschner A, Federici G and Kukushkin A 2009 *Journal of Nuclear Materials* **390-391** 1–9 ISSN 0022-3115 URL http://www.sciencedirect.com/science/article/pii/S0022311509000506

[72] Nordlund K, Djurabekova F and Hobler G 2016 *Physical Review B* **94** 214109 URL https://link.aps.org/doi/10.1103/PhysRevB.94.214109

[73] Roth J, Eckstein W and Guseva M 1997 *Fusion Engineering and Design* **37** 465–480 ISSN 0920-3796 URL http://www.sciencedirect.com/science/article/pii/S0920379697000914

[74] Wert C and Zener C 1949 *Physical Review* **76** 1169–1175 URL https://link.aps.org/doi/10.1103/PhysRev.76.1169

[75] Ziegler J F, Ziegler M D and Biersack J P 2010 *Nuclear Instruments and Methods in Physics Research Section B: Beam Interactions with Materials and Atoms* **268** 1818–1823 ISSN 0168-583X www.srim.org URL http://www.sciencedirect.com/science/article/pii/S0168583X10001862

[76] Los J H, Zakharchenko K V, Katsnelson M I and Fasolino A 2015 *Physical Review B* **91** 045415 URL https://link.aps.org/doi/10.1103/PhysRevB.91.045415

[77] Hernández E, Goze C, Bernier P and Rubio A 1998 *Physical Review Letters* **80** 4502–4505 URL https://link.aps.org/doi/10.1103/PhysRevLett.80.4502

[78] Hsieh J Y, Lu J M, Huang M Y and Hwang C C 2006 *Nanotechnology* **17** 3920 ISSN 0957-4484 URL http://stacks.iop.org/0957-4484/17/i=15/a=051